

High-Speed Event Vision-Based Tactile Roller Sensor for Large Surface Measurements

Akram Khairi¹, Hussain Sajwani¹, Abdallah Mohammad Alkilany¹, Laith AbuAssi¹, Mohamad Halwani¹, Islam Mohamed Zaid¹, Ahmed Awadalla¹, Dewald Swart², Abdulla Ayyad¹, Yahya Zweiri¹

Abstract—Inspecting large-scale industrial surfaces like aircraft fuselages for quality control requires capturing their precise 3D surface geometry at high resolution. Vision-based tactile sensors (VBTSs) offer high local resolution but require slow ‘press-and-lift’ measurements stitched for large areas. Approaches with sliding or roller/belt VBTS designs provide measurements continuity. However, they face significant challenges respectively: sliding struggles with friction/wear and both approaches are speed-limited by conventional camera frame rates and motion blur, making large-area scanning time consuming. Thus, a rapid, continuous, high-resolution method is needed. We introduce a novel tactile sensor integrating a neuromorphic camera in a rolling mechanism to achieve this. Leveraging its high temporal resolution and robustness to motion blur, our system uses a modified event-based multi-view stereo approach for 3D reconstruction. We demonstrate state-of-the-art scanning speeds up to 0.5 m/s, achieving Mean Absolute Error below 100 microns – 11 times faster than prior continuous tactile sensing methods. A multi-reference Bayesian fusion strategy enhances accuracy (reducing MAE by 25.2% compared to EMVS) and mitigates curvature errors. We also validate high-speed feature recognition via Braille reading 2.6 times faster than previous approaches.

I. INTRODUCTION

Surface metrology and surface inspection are crucial elements in quality assurance across diverse industries, particularly aerospace and automotive manufacturing. Precise inspection is required to identify characteristics like paint quality, coating integrity, and subtle defects such as cracks, nicks, and dents [1], [2], [3]. Often, achieving a resolution of 0.1 mm or lower is necessary to accurately classify these features and ensure component integrity and safety [4]. Traditional contact-based methods, including high-precision profilometers [5], [6] or microscopic techniques [7], [8], [9], offer high resolution locally but become exceedingly time-consuming when applied to large surface areas due to their sequential, point-by-point or small-patch measurement nature. Non-contact optical methods, such as cameras, laser scanners, or structured light systems [2], [10], [11], [12], [13], [14], can significantly accelerate inspection by capturing data over wider areas. However, these methods often lack robustness; their performance can be compromised by variations in ambient lighting, motion blur when attempting high-speed scanning, or challenging surface optical properties like high reflectivity or transparency [15]. This

highlights a critical need for sensing modalities that combine high resolution and robustness with the capability for rapid inspection of large, potentially complex surfaces.

Vision-Based Tactile Sensors (VBTSs), particularly those derived from the GelSight concept [3], [16], [17], have emerged as a powerful contact-based alternative offering a unique blend of high-resolution geometric and textural sensing. These sensors typically employ a camera to view the deformation of a soft, reflective elastomer membrane pressed against a target surface. This principle allows for detailed surface capture, often with inherent robustness to external lighting conditions due to internal illumination [3], [18]. Numerous variations of GelSight have been developed, enhancing capabilities for robotic manipulation, complex shape capture, and integration into compact form factors [19], [20], [21], [22].

Despite their advantages for detailed local analysis, the standard planar configuration of most VBTSs necessitates a discrete “press-and-lift” interaction mode. This process, where the sensor is repeatedly pressed, lifted, and moved, becomes prohibitively time-consuming when inspecting large surface areas, requiring numerous measurements to be stitched together [4], thereby limiting their use for efficient large-scale tactile measurement.

To enable continuous tactile measurement, various designs moving beyond the static planar configuration have emerged. Attempts at direct sliding of planar sensors face significant friction, wear, and motion blur challenges [23]. Roller-based [24], [25] and belt-based [26] VBTS designs replace the static contact with a dynamic rolling interface, allowing continuous data acquisition. TouchRoller, for example, demonstrated 2D texture mapping over moderate areas [24], while GelBelt provides a larger contact patch via its belt mechanism [26]. Despite these mechanical advancements for measurement continuity, these designs face limitations. Reconstructing accurate 3D geometry from the depth-variant information gathered by cylindrical rollers is complex, primarily because the contact depth is not uniform across the curved sensing area. This variation distorts the captured tactile image and complicates the mapping between observed elastomer deformation and the actual 3D surface geometry [27]. More critically, the operational speed of systems relying on conventional cameras is constrained. Frame rate limitations and motion blur become significant issues as scanning speed increases. This problem is particularly acute for VBTS, which often require close-up imaging with a shallow depth of field to resolve fine surface details; any slight vibration

¹ Advanced Research and Innovation Center (ARIC), Khalifa University, Abu Dhabi, United Arab Emirates

² Research and Development, Strata Manufacturing PJSC, Al Ain, United Arab Emirates

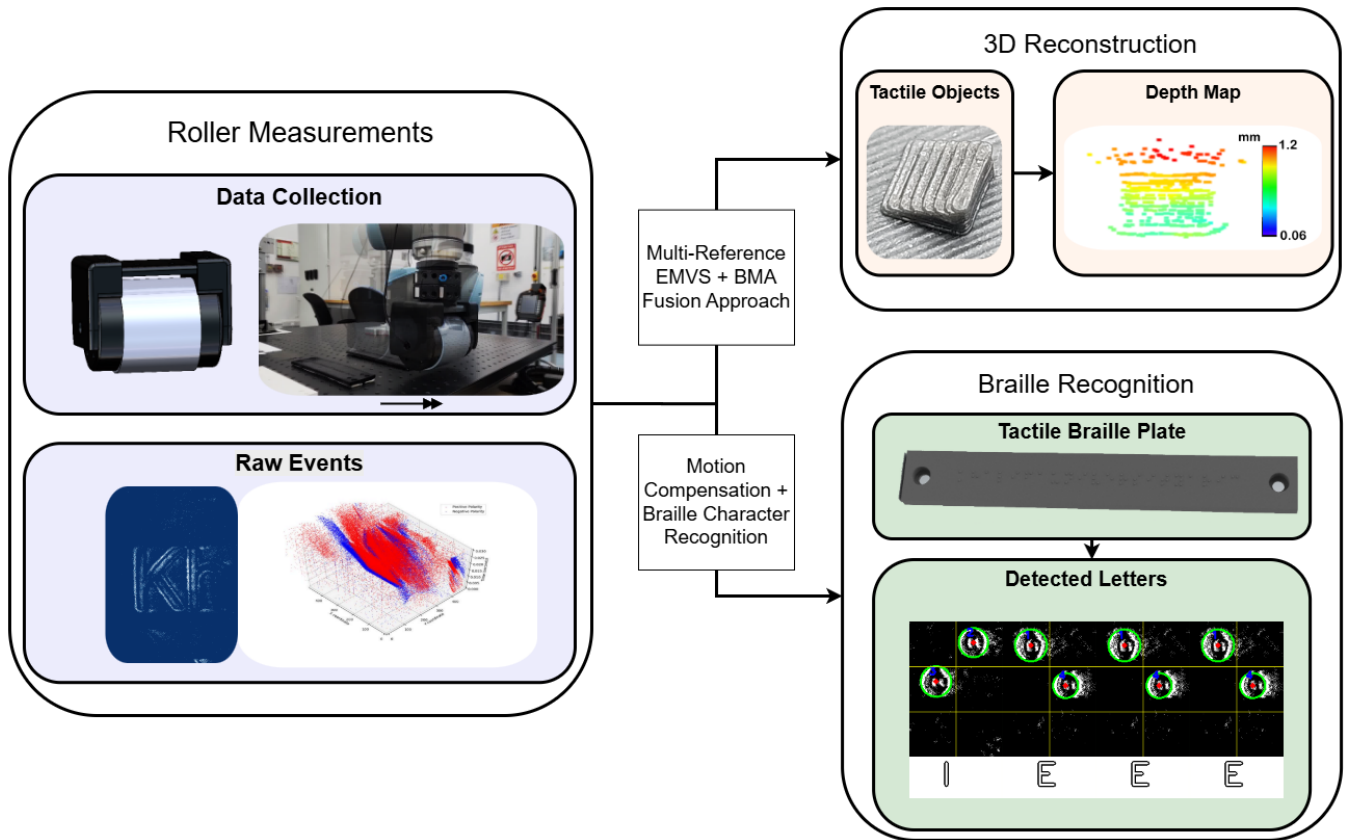


Fig. 1. The proposed neuromorphic roller tactile sensor enables high-speed surface analysis. The system (mounted on UR10 robotic arm) captures asynchronous events during continuous rolling (left) and utilizes event-based algorithms for both 3D surface reconstruction (top right) and fine feature recognition, demonstrated via Braille reading (bottom right), surpassing the speed limitations of conventional tactile methods for large surface inspection.

during the camera’s exposure time at high speeds drastically worsens motion blur, degrading reconstruction accuracy. Consequently, current roller/belt tactile sensors are restricted to relatively low velocities (e.g., typically well below 0.1 m/s for 3D reconstruction [24], [26]), insufficient for truly high-throughput industrial inspection of large parts.

Neuromorphic vision sensors, or event cameras, provide a promising technological solution to overcome these speed barriers [28], [29]. Unlike frame-based cameras, event cameras feature pixels that respond independently and asynchronously to logarithmic brightness changes, generating data with microsecond-level temporal resolution, high dynamic range, and inherent resistance to motion blur [30], [31], [32]. These characteristics are ideally suited for capturing the rapid, dynamic deformations occurring at the contact interface of a high-speed rolling tactile sensor. Crucially, integrating event cameras into tactile roller designs holds considerable potential for achieving high-resolution continuous tactile sensing at higher speeds with significantly lower computational power, particularly for surfaces with sparse details, compared to conventional VBTSs. While Neuromorphic VBTSs (NVBTS) have been explored for applications like robotic grasping and slip detection (e.g., Evetac [33]) or contact analysis [34], [35], [36], [37], their potential for enabling high-speed, continuous 3D large surface reconstruction using a roller mechanism has not been realized. A

significant gap exists for a tactile sensing system capable of combining the continuous scanning geometry of a roller with the high temporal fidelity and motion robustness of event-based vision for large-scale surface measurement.

This paper introduces, to the best of our knowledge, the first high-speed neuromorphic vision-based roller tactile sensor specifically designed for large surface measurements (illustrated in Figure 1). Our primary contributions are:

- 1) We present the first work demonstrating the use of a neuromorphic vision-based tactile sensor (NVBTS) for high-resolution 3D reconstruction and surface inspection.
- 2) We present a novel rolling neuromorphic vision-based tactile sensor for 3D reconstruction and feature recognition of surfaces at speeds reaching up to 0.5 m/s, 11 times faster than the previous approaches.
- 3) We propose a modified event-based multi-view Stereo (EMVS) algorithm. Our approach enhances depth estimation and consistency on curved tactile sensors by fusing depth maps from multiple reference views. Furthermore, we include a corresponding calibration routine to optimize its parameters.
- 4) We rigorously test the proposed roller-based tactile sensor (RBTS) in 3D reconstruction tasks and compare its performance against the state-of-the-art for large surface inspection with regards to speed and accuracy.

II. RELATED WORKS

A. 3D Surface Reconstruction

Reconstructing a surface’s three-dimensional geometry is crucial in many applications, from automated manufacturing to quality control. Mechanical profilometers have long been used for high-precision surface measurements, meticulously tracing the surface point-by-point. However, this inherent sequential nature makes them slow, especially when dealing with complex geometries or large areas [6]. Non-contact optical techniques, like laser scanning and structured light, offer a significant speed advantage by rapidly capturing surface data over a wider area [38], [39]. These methods boast resolutions around 0.1 mm [16], but their reliance on light makes them susceptible to issues with highly reflective or transparent materials, as well as variations in ambient lighting conditions [15]. Furthermore, certain laser scanning systems, particularly higher-power ones used for speed or range, can introduce eye-safety concerns requiring adherence to safety standards and protocols [40].

For applications demanding the utmost precision, techniques like white light interferometry, confocal microscopy, and atomic force microscopy (AFM) are utilized [7], [8], [9]. These methods can resolve surface details down to the nanometer scale, revealing intricate textures and features. However, they often involve complex setups, lengthy measurement times, and significant expense, limiting their practical use for large-scale inspection tasks.

B. Vision-Based Tactile Sensors

Vision-Based Tactile Sensors (VBTSs) have emerged as compelling alternatives for surface sensing, offering robustness, versatility, and ease of use. The GelSight sensor pioneered this field, making use of a soft, deformable surface with camera-based observation to extract detailed surface information utilizing photometric stereo [16]. By analyzing the deformation of the elastomer, typically coated with a reflective layer, VBTSs can capture high-resolution data on surface geometry and texture, even under varying lighting [3], [18]. From the original GelSight concept, a diverse range of VBTS designs have emerged to enhance performance and broaden application: GelSlim for more compact integrations [19], GelSight Fin Ray for soft compliant grippers [20], and GelSight Svelte for human shape mimicking [21] to name a few. Crucially, simulation tools have evolved in parallel, accelerating the design and deployment of novel VBTS solutions [41], [42], [43], [44].

However, conventional VBTSs often face challenges when it comes to continuous surface scanning. The rigid backing of the elastomer limits its ability to slide smoothly across the surface, leading to distortions and potential damage to the sensing membrane. Consequently, these sensors often require a discrete “press-and-lift” approach, making them ill-suited for rapid inspection of large areas; for example, the commercial GelSight Mobile™ Series 2 requires approximately 0.1 seconds of exposure time per measurement patch [45], rendering large area coverage time-consuming [4]. An attempt to address this limitation using continuous

sliding with a conventional VBTS (DIGIT) was explored by Potdar et al. for high-speed Braille reading [23]. While demonstrating the potential for sliding interactions, their approach, relying on a conventional camera, encountered significant motion blur artefacts at higher velocities, leading to a notable decrease in recognition accuracy as the sliding speed increased. Furthermore, the inherent friction during sliding poses a significant challenge for conventional VBTS elastomers, potentially causing rapid wear or damage to the delicate sensing surface, an issue Potdar et al. mitigated partially through the use of protective tape [23]. While reducing wear, such protective layers can introduce optical diffusion, potentially limiting the resolution of very fine textures, and may necessitate more precise control over maintaining perpendicular contact during sliding to ensure consistent data acquisition.

C. Neuromorphic Vision-Based Tactile Sensing

Neuromorphic vision sensors, or event cameras, offer a transformative technology for high-speed tactile sensing by directly addressing the limitations of conventional cameras [28]. Their asynchronous pixel operation leads to microsecond temporal resolution, high dynamic range, low latency, and inherent suppression of motion blur [30], [31], [32]. These properties are exceptionally well-suited to capturing the rapid, dynamic changes in elastomer deformation during high-speed continuous tactile scanning. Several Neuromorphic VBTSs (NVBTS) have leveraged these advantages. Initial explorations included using Gaussian processes on event data for contact force estimation [46] or employing spiking neural networks (SNNs) for texture classification (NeuroTac [34]), though SNNs can be challenging to train for regression tasks like pose or force prediction. More recent systems like Evetac [33] utilize event-based marker tracking for robust slip detection during robotic grasping, demonstrating the utility of events for dynamic contact analysis. Graph neural networks have been applied to event streams for contact angle prediction (Tactigraph [35]), and other works have explored generating image-like representations from events for proprioception or other analyses [36]. While these studies validate the potential of NVBTS, their focus has predominantly been on grasping-related tasks (slip, force, contact classification) or local texture analysis. Moreover, for these use cases, most NVBTS suffer from decreased spatial resolution due to the reliance on markers, which is detrimental for surface reconstruction and depth estimation [33].

D. Roller-Based and Large Surface Tactile Sensors

Roller-based tactile sensors represent a promising avenue for achieving continuous tactile sensing, particularly for large surfaces where traditional planar sensors are inefficient. Early work explored cylindrical designs for specific detection tasks, such as the sensor developed by Shimonomura et al. [25] for detecting foreign bodies like food impurities during rolling contact. Similarly, studies in robotic in-hand manipulation have successfully utilized a roller grasper, often

equipped with high-resolution tactile feedback, for tasks like object insertion and regrasping [47], [48], demonstrating the utility of rolling contact in dynamic scenarios beyond simple surface mapping.

Transitioning towards surface property characterization, TouchRoller [24] demonstrated the potential for mapping surface textures by continuously rolling a sensor element across a fabric sample. It achieved coverage of an $8\text{cm} \times 11\text{cm}$ area in 10 seconds, yielding a 2D texture map. Notably, its operational speed was limited to approximately 11 mm/s; the authors noted that higher speeds resulted in motion blur within the conventional camera frames, hindering performance. This motion blur problem is particularly acute for VBTs, which require close-up imaging to resolve fine surface details. Operating at such close proximity means that even moderate rolling speeds translate into high velocities of features across the image sensor plane; during the camera's finite exposure time, these features traverse a larger number of pixels, resulting in significant motion blur compared to imaging from a distance. Furthermore, TouchRoller did not perform 3D surface reconstruction. Addressing 3D reconstruction, GelRoller [49] employed a cylindrical design integrating photometric stereo techniques for local surface normal estimation from single frames. For reconstructing larger surfaces, they proposed stitching multiple local reconstructions using Iterative Closest Point (ICP) registration. While demonstrating 3D capability, this work did not explicitly analyze or optimize the operational speed of the rolling process.

A fundamental challenge inherent to cylindrical roller designs, however, is that the tactile information gathered varies significantly with contact depth due to the sensor's curvature. This leads to inconsistencies and potential distortions in the acquired tactile images, complicating accurate reconstruction. Researchers have explored methods to mitigate this depth inconsistency. Li et al. [27] proposed a cyclic image fusion strategy, processing information from different contact phases within the rolling sequence using wavelet transforms to enhance information extraction and reduce bias from the curved contact.

An alternative approach addresses the issue mechanically: the GelBelt sensor [26] utilizes a flat elastomeric belt moving between two wheels, creating a larger, more uniform contact area akin to a conveyor. This design avoids the depth variation inherent in direct cylindrical contact and enabled continuous sensing at higher reported speeds, up to 45 mm/s. However, this design comes with some drawbacks. It relies on sliding motion to achieve high-speed operation, using an air gap and a smooth surface to reduce friction. While this allows GelBelt to move quickly, it creates challenges for lighting and can lead to wear over time, which may affect the system's accuracy and repeatability. The design also struggles with curved surfaces. Its large, flat structure makes it hard to access concave areas, and it doesn't perform well on convex surfaces either. In this case, the flat sensor doesn't match the shape of the curved surface, leading to a limited sensing area, similar to problems seen in roller-based systems.

Furthermore, despite these advances in measurement continuity, including GelBelt's increased speed, systems relying on conventional cameras remain fundamentally constrained by the trade-off between speed and accuracy due to motion blur. As demonstrated by GelBelt's own results showing decreased accuracy at higher speeds [26], pushing scanning velocities further significantly degrades the quality of the captured tactile information and subsequent reconstructions. While naively increasing camera frame rates might seem like a straightforward solution to combat motion blur, it introduces substantial challenges regarding the increased computational complexity required for real-time processing, significantly larger data storage requirements, and higher energy consumption, potentially limiting practical deployment. In turn, the potential for using event-based vision in roller sensors to achieve similar resolution at low computational power and significantly higher speeds for continuous tactile sensing is considerable. However, this capability has yet to be demonstrated, particularly for demanding large-scale inspection tasks.

III. METHODOLOGY

A. Mechanical Design and Fabrication

As illustrated in Figure 2a, our proposed sensor consists of: a clear, transparent acrylic cylinder as a support structure; a translucent elastomer with a reflective coating; a neuro-morphic camera (DVXplorer mini); a white LED ring with diffuser; shafts that attach to the camera holder; bearings to keep the camera holder stationary during rolling; and sealing covers to attach the cylinder and shafts to the outer housing as well as seal the light from the LEDs within the sensor.

The acrylic cylinder is cut to 100 mm in length, and the elastomer covers 80 mm of the cylinder. The elastomer layer coated with the reflective membrane covers a portion of the cylinder. When an object makes contact with the elastomer, the soft elastomer will deform. The camera will capture the deformation with the help of the reflective membrane and the illumination provided by the internal LEDs. Crucially, unlike photometric stereo methods which require precisely calibrated and stable illumination to infer shape from shading, our approach utilizes Event-Based Multi-View Stereo (EMVS). This method reconstructs 3D structure by tracking the apparent motion of features across multiple viewpoints as the sensor rolls (Structure from Motion). In turn, the system is inherently more robust to variations in illumination intensity or minor inconsistencies in LED positioning compared to the photometric stereo approach adopted by most VBTs.

The camera is mounted and secured in the camera holder within the cylinder, with the entire sensor having dimensions of L: 116 mm, W: 148 mm, and H: 88 mm, with the elastomer being 47 mm in radius. The sensing area is around 40 by 30 mm.

The fabrication process begins with the elastomer. The elastomer is expected to be soft so that it is able to respond to contact even with a small force, and translucent so that the light can be reflected properly from the sensing area to

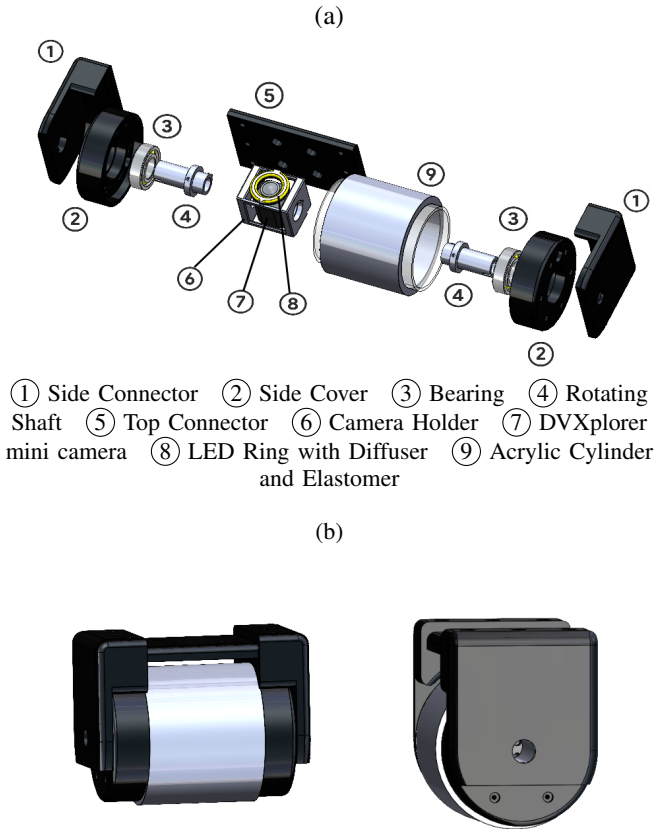


Fig. 2. Mechanical Design of Roller: (a) Exploded view of roller components; (b) Front view (left) and side view (right) of assembled roller.

the camera. For the fabrication of the elastomer, Smooth-On Sorta-Clear 18 with Shore A Hardness of 18 was used. Part A: Part B ratio was 10:1 as recommended by the manufacturer. A mold was 3D printed with two concentric acrylic cylinders to ensure a smooth outer surface for the elastomer and the cylinders were removed once curing was done.

Once the elastomer has cured and demolded, the reflective coating is applied consisting of: Inkcups Clear SI Ink, Hardener, Solvent, and silver mica powder in the ratios 8:1:1:1 respectively. The ink coating is then placed on the elastomer with a rotary silk screen printing machine and left to dry in an oven at 100°C for 10 mins as recommended by Inkcups to bond with the silicone elastomer.

The supporting parts, which were used to connect all the components, consisted of shafts, a camera holder, and sealing covers. The other components (shafts, camera holder, sealing covers) were 3D printed with PLA. Lastly, brass inserts and screws were used to secure the components together. The final assembled roller is shown in Figure 2b.

B. Event Camera Principles

Unlike conventional cameras that capture intensity information across all pixels at fixed frame rates, event cameras employ a fundamentally distinct, bio-inspired sensing

paradigm [28]. Each pixel operates independently and asynchronously, responding dynamically to changes in illumination. Specifically, a pixel monitors the logarithm of the incident light intensity, $L(x, y, t) = \log(I(x, y, t))$. An event $e_k = (x_k, y_k, t_k, p_k)$ is generated at coordinates (x_k, y_k) only when the change in this logarithmic intensity, ΔL , relative to its value at the time of the last event from that pixel, surpasses a predefined contrast threshold, $\pm C$. The generated event includes a high-resolution timestamp t_k and a polarity $p_k \in \{-1, +1\}$, signifying the direction of the brightness change (decrease or increase, respectively). Following event generation, the pixel's internal reference brightness level is updated, priming it for subsequent intensity variations. The output is thus not a sequence of frames, but a sparse, continuous stream of asynchronous events reflecting dynamic scene changes. The unique characteristics of event cameras offer substantial benefits for high-speed tactile inspection. Their inherent high temporal resolution, with events timestamped often at microsecond precision, allows for tactile sensing at high speeds without the motion blur experienced by other roller tactile sensors at similar speeds. Furthermore, event-based cameras benefit from low latency and high dynamic range allowing for potential reduction in computational load and robustness to varying illumination within the sensor housing respectively.

C. Surface Reconstruction

1) *Event-Based Multi-View Stereo (EMVS)*: In motion parallax, objects closer to the observer (or camera) appear to move faster across the field of view than objects farther away. This effect is due to the relative difference in angular displacement caused by motion, and it's a key depth cue used by both biological and artificial vision systems to perceive 3D structure from motion. To estimate the 3D structure of the scanned surface from the event stream generated by the moving roller, we adapt the multi-view stereo (MVS) space-sweep method, originally developed for frame-based cameras [50] and later extended to event cameras (EMVS) [51]. This technique leverages the known viewpoints (poses) of the event camera over time. The core idea involves discretizing a volume of interest, $\bar{D} \in \mathbb{R}^{w \times h \times N_z}$, encompassing the potential 3D scene, where w , h , and N_z represent the dimensions of the volume. Each captured event, $e_k = (x_k, y_k, t_k, p_k)$, is back-projected through this volume as a 3D ray using the camera's calibrated intrinsic parameters and its known pose at time t_k .

A Disparity Space Image (DSI) is employed to accumulate evidence for surfaces within the volume. The DSI acts as a 3D histogram where each voxel counts the number of back-projected event rays passing through it, typically referenced to a specific viewpoint. Voxels corresponding to real surfaces in the scene are expected to lie at the intersection of rays from multiple viewpoints, resulting in high ray counts. Local maxima in the ray density within the DSI are then identified as potential 3D points belonging to the scanned surface [51], [52]. Processing these maxima using Adaptive Gaussian Thresholding, yields a semi-dense depth map relative to the reference viewpoint.

2) Multi-Reference Depth Map Generation and Fusion:

The standard EMVS approach generates a depth map referenced to a single key viewpoint, often chosen as the midpoint $t_m = (t_s + t_e)/2$ within a processing time window $[t_s, t_e]$. We select a time window of 20 ms, balancing the need for sufficient event integration for reconstruction accuracy with the requirement for high-speed operation (up to 0.5 m/s) without introducing significant motion artifacts in the DSI.

However, roller-based tactile sensing can suffer from errors due to the sensor's curved nature, leading to inconsistent contact depth and potential fabrication variations [53]. High-speed motion can also introduce occlusion and warping artifacts. To enhance robustness against these effects and specifically mitigate the depth inconsistency and curvature-induced errors inherent in cylindrical tactile sensing, we extend the EMVS framework by generating and fusing depth maps from multiple reference times within the same time window. Inspired by works demonstrating the benefits of multi-reference objectives in event-based vision [54] and fusion techniques in roller tactile sensing [53], our approach specifically computes depth maps Z_s , Z_m , and Z_e referenced at the start (t_s), midpoint (t_m), and end (t_e) times of the window, respectively. As demonstrated quantitatively and qualitatively in the Results section (Section V, Figure 9), this fusion strategy significantly improves depth consistency and reduces depth map curvature distortion compared to EMVS.

We propose fusing these individual depth maps using a Bayesian Model Averaging (BMA) strategy (Figure 3), which has proven effective for combining multiple noisy estimates in vision tasks [55]. The fused depth map, Z_f , is computed as a weighted average of the individual depth maps after warping them to a common reference frame (chosen as the midpoint view, t_m):

$$Z_f = \sum_{i \in \{s, m, e\}} w_i \cdot W_i(Z_i) \quad (1)$$

where Z_i is the depth map generated at reference time t_i , w_i is the corresponding fusion weight, and W_i is the warping function. The warping function W_i relies on standard camera projection models. Event cameras utilize the same optical principles as traditional cameras, allowing the use of the pinhole projection model to relate 3D world points to 2D image points. A 3D point $\mathbf{P}_W = [X_W, Y_W, Z_W]^T$ in the world frame is projected onto the image plane as a 2D pixel $\mathbf{p} = [u, v, 1]^T$ according to:

$$z\mathbf{p} = \mathbf{K}[\mathbf{R}|\mathbf{t}] \begin{bmatrix} \mathbf{P}_W \\ 1 \end{bmatrix} = \mathbf{K} \begin{bmatrix} \mathbf{P}_C \\ 1 \end{bmatrix} \quad (2)$$

where z is the depth Z_C of the point in the camera frame, \mathbf{K} is the 3×3 camera intrinsic matrix, $[\mathbf{R}|\mathbf{t}]$ represents the 3×4 extrinsic matrix (rotation \mathbf{R} and translation \mathbf{t}) transforming world coordinates to camera coordinates $\mathbf{P}_C = [X_C, Y_C, Z_C]^T$. The absolute pose of the camera frame relative to the robot base frame, ${}^B\mathbf{T}_C(t)$, which defines \mathbf{R} and \mathbf{t} relative to the base frame at time t , is obtained by combining the robot's end-effector pose ${}^B\mathbf{T}_E(t)$ (derived from forward kinematics) with the fixed hand-eye transformation ${}^E\mathbf{T}_C$,

determined via hand-eye geometric calibration [52]. The intrinsic matrix \mathbf{K} is also obtained through calibration using E-Calib, a calibration toolbox for event cameras [56].

The warping process transforms the depth value associated with a pixel $\mathbf{p}_i = [u, v, 1]^T$ in the image plane at time t_i to the corresponding pixel location $\mathbf{p}' = [u', v', 1]^T$ in the image plane at the common reference time t_m . Specifically, this involves three steps:

- 1) **Back-projection:** A pixel \mathbf{p}_i with depth $Z_i(u, v)$ from the depth map at time t_i is back-projected to its corresponding 3D point $\mathbf{P}_i = [X_i, Y_i, Z_i]^T$ in the camera's coordinate frame at t_i using the inverse pinhole projection:

$$\mathbf{P}_i = Z_i(u, v)\mathbf{K}^{-1}\mathbf{p}_i \quad (3)$$

- 2) **Transformation:** The 3D point \mathbf{P}_i is transformed into the camera's coordinate frame at the reference time t_m using the relative pose transformation ${}^m\mathbf{T}_i$, which is calculated from the absolute poses as ${}^m\mathbf{T}_i = ({}^B\mathbf{T}_C(t_m))^{-1} \cdot {}^B\mathbf{T}_C(t_i)$. Using homogeneous coordinates:

$$\begin{bmatrix} \mathbf{P}_m \\ 1 \end{bmatrix} = {}^m\mathbf{T}_i \begin{bmatrix} \mathbf{P}_i \\ 1 \end{bmatrix} \quad (4)$$

where $\mathbf{P}_m = [X_m, Y_m, Z_m]^T$ is the point in the reference frame m .

- 3) **Re-projection:** The transformed 3D point \mathbf{P}_m is projected back onto the image plane at time t_m to find the warped pixel coordinates $\mathbf{p}' = [u', v', 1]^T$:

$$Z_m\mathbf{p}' = \mathbf{K}\mathbf{P}_m \quad (5)$$

The original depth value $Z_i(u, v)$ is then associated with the calculated warped pixel location (u', v') in the reference frame m before the weighted averaging (Eq. 1) is performed.

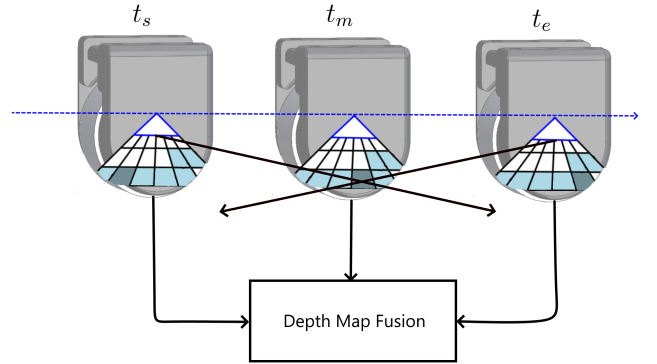


Fig. 3. Multi-Reference Fusion Strategy: For each reference time, each incoming ray from a back-projected event counter votes for the voxels it passes through in the corresponding DSI ray counter. Depth map is extracted from each DSI and these depth maps are fused using BMA.

D. Parameter Calibration

To optimize the final reconstruction quality, we perform a one-time calibration using an object with precisely known geometry, specifically a sphere of known radius R_{sphere} . This calibration determines the optimal values for both the

adaptive thresholding parameters used in processing the DSI and the fusion weights used in combining multi-reference depth maps. The adaptive thresholding parameters (constant C and median filter size G_f) control the density and noise level of the individual depth maps Z_i , while the fusion weights w_s, w_m, w_e dictate how these maps are combined into the final estimate Z_f . Furthermore, this calibration procedure can be readily repeated in-situ, enabling the system to adapt to gradual changes in the elastomer surface, such as wear, by re-optimizing these parameters.

To establish the ground truth depth map Z_{gt} for the sphere contact, we adapt the methodology used in [49]. When the calibration sphere is pressed onto the sensor, we first identify the resulting circular contact patch in the depth map (visualized in Figure 4). From this, we determine the radius of the pressed circle, r (in pixels), and the coordinates of its center, (x_b, y_b) (in pixels). The depth of the sphere’s center, z_b (in pixels), can be calculated geometrically as:

$$z_b = -\sqrt{(R_{sphere})^2 - r^2} \quad (6)$$

For any pixel (x_i, y_i) within the identified contact circle, its depth z_i (in pixels) must satisfy the sphere equation:

$$(x_i - x_b)^2 + (y_i - y_b)^2 + (z_i - z_b)^2 = (R_{sphere})^2 \quad (7)$$

Solving Equation 7 for z_i for all pixels inside the contact circle yields the ground truth depth map in pixel units. This map is then converted to millimeters to obtain Z_{gt} by multiplying with the scale factor f . We determined this scale factor $f = 0.0422$ mm/pixel by imaging features of known dimensions using a Vernier caliper (varying space between jaws from 2 to 5 mm and averaging results).

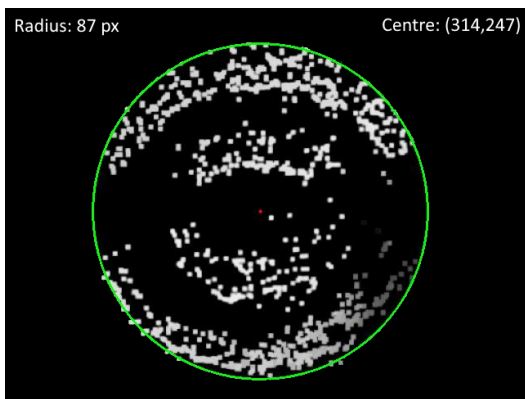


Fig. 4. Identification of the circular contact patch from depth map during calibration with the 4mm radius sphere. The green circle outlines the detected boundary, from which the contact radius r and center (x_b, y_b) (red dot) are determined in pixel coordinates.

With the ground truth Z_{gt} established, both sets of parameters (thresholding and fusion weights) are optimized simultaneously by minimizing the Mean Absolute Error (MAE) between the final fused depth map Z_f and Z_{gt} . A region mask corresponding to the sphere’s contact area is applied before calculating the MAE. The optimization is performed via a grid search over the combined parameter

space:

$$\min_{\theta} \mathbb{E}[\|Z_f - Z_{gt}\|_1] \quad (8)$$

where $\theta = \{C, G_f, w_s, w_m, w_e\}$. The range and optimal values for each parameter can be seen in Table I.

TABLE I
PARAMETER RANGES AND OPTIMAL CALIBRATED VALUES

Parameter	Range	Optimal Value
C	5–20	16
G_f	11–91	45
w_m	0–1	0.333
w_s	0–1	0.445
w_e	0–1	0.222

The calibrated values for all parameters are subsequently fixed and utilized for processing the data from all other scanned objects presented in this work. The effect of calibration on the processed depth map and point cloud are shown in Figure 5. From a Bayesian perspective, the optimal weights should ideally be inversely proportional to the uncertainty associated with each individual depth map Z_i , effectively giving more influence to more confident estimates.

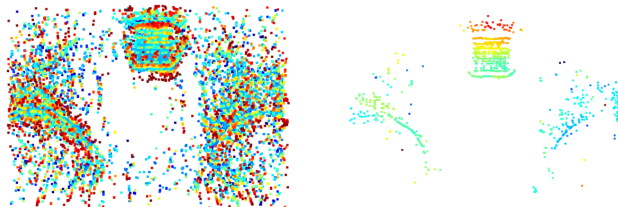


Fig. 5. Comparison of pointcloud processed with EMVS: before calibration (left) and after calibration (right). The pointcloud processed with calibrated parameters has significantly less noisy events particularly around the tactile object of interest. Color represents change in depth using JET colormap.

E. Cross-Validation and Weighted Fusion Analysis

A potential concern is that the optimal fusion weights determined using only the sphere geometry might be biased and not generalize well to other object shapes (outlined in detail in Section IV). To investigate this, we performed a cross-validation analysis. We first determined the object-specific optimal fusion parameters θ_i (the weights w_s, w_m, w_e were highlighted since the thresholding parameters did not change across objects) by running the grid search optimization (Eq. 8) using the ground truth $Z_{gt}^{(i)}$ for each object i (where $i \in \{\text{Sphere, Stairs, Sparse Sphere}\}$).

We then evaluated how well each set of parameters θ_i performed on average across all $M = 3$ test objects. For each candidate parameter set θ_i (calibrated on object i), we calculated its average MAE, e_i , across all test objects j as follows:

$$e_i = \frac{1}{M} \sum_{j=1}^M \|Z_f^{(j)}(\theta_i) - Z_{gt}^{(j)}\|_1 \quad (9)$$

where $Z_f^{(j)}(\theta_i)$ is the fused depth map generated for object j using parameters θ_i . We then compared these average error values to determine which calibration object yielded the parameters with the best overall generalization performance (i.e., the minimum e_i).

The results are summarized in Table II. While the object-specific optimal weights vary slightly, the weights calibrated using the sphere yielded the lowest overall average MAE ($e_{\text{Sphere}} = 0.0549$ mm) when applied universally, confirming its suitability as a general calibration target.

TABLE II
CROSS-VALIDATION OF BMA FUSION WEIGHTS

Calibrated on	w_s	w_m	w_e	Avg. MAE (mm)
Sphere	0.445	0.333	0.222	0.0549
Stairs	0.5	0.333	0.167	0.0652
Sparse Sphere	0.4	0.4	0.2	0.0649

A consistent and perhaps counter-intuitive trend observed across all calibrations is that the start reference view (t_s) receives the highest (or tied for highest) weight, while the end view (t_e) consistently receives the lowest. Intuitively, one might expect the midpoint view (t_m), representing a temporal average, to be most reliable. However, this weighting suggests the information captured early in the time window is most critical for accurate reconstruction in our setup. Several factors related to the EMVS algorithm and rolling contact dynamics may contribute:

- **Pose Confidence:** The pose at t_s is derived directly from the robot state at the window’s beginning. The pose at t_m relies on interpolation and assumes constant velocity within the 20ms window, therefore there could be a disparity between the interpolated pose and actual pose at t_m . The estimated pose at t_e may carry slightly greater uncertainty than at t_s , stemming from both potential inaccuracies in interpolating the robot pose between controller updates to match precise event timestamps, and the manifestation of small kinematic errors or unmodeled dynamic effects during the 20ms motion interval. Thus, the geometric reference at t_s might be inherently the most accurate relative to the events occurring near it.
- **Information Content:** As the roller moves, tactile features first appear and generate events with high contrast near the start of the window (t_s). This information might provide the most stable features for the EMVS algorithm before potential disocclusions occur. Conversely, features rolling out of view near t_e might contribute less reliable data or introduce artifacts.
- **Error Accumulation in DSI:** The DSI integrates events over the entire window. Errors in pose estimation or event timing later in the window could slightly degrade the DSI’s quality relative to the t_e viewpoint compared to its quality relative to the t_s viewpoint.

Overall, the results strongly suggest that the initial phase of the time window provides the most pertinent information for robust reconstruction via EMVS for this high-speed tactile

rolling application.

F. Braille Feature Recognition

To demonstrate the sensor’s capability for fine feature detection at high speed, we implemented a Braille character recognition pipeline. The process begins by applying motion compensation [10], [57] to the recorded event stream as the sensor rolls over the Braille plate. Given the constant linear velocity of the roller, v_{roller} , which is commanded to and precisely controlled by the UR10 robotic arm as described in the Experimental Setup (Sec. IV), we can determine the corresponding optical flow $\dot{\mathbf{U}} = (\dot{u}, \dot{v})$ of features moving across the image plane with $[u, v]$ as the pixel coordinates. The roller’s motion involves predominantly horizontal motion, therefore $\dot{v} \approx 0$ and $\dot{u} = \frac{F}{Z}v_{\text{roller}}$, where F is the focal length of the camera and Z is the depth of the scene (assumed to be constant depth of 47 mm which is the radius of the roller with maximum deformation of 4.5 mm).

Without motion compensation, if we were to simply create a frame-like image by plotting all events recorded within a specific time window at their original pixel locations (a process called direct accumulation), the relative movement between the sensor and the Braille plate would cause significant motion blur. This occurs because events generated by a single point on the moving Braille surface would be spread across multiple pixels in the resulting image (as seen in Figure 6a). Using a long accumulation time integrates more events but exacerbates this blur as features traverse many pixels, whereas a very short accumulation time minimizes blur but often captures too few events to form a clear representation, leading to degraded features [10], [57]. To counteract this, we warp events with batches consisting of a constant number of events ($N_e = 20,000$ events) at the initial timestamp of the event stream as the reference time, t_{ref} . For each event $e_k = (\mathbf{x}_k, t_k, p_k)$ where $\mathbf{x}_k = (x_k, y_k)$, its warped position \mathbf{x}'_k is calculated as:

$$\mathbf{x}'_k = \mathbf{x}_k - \dot{\mathbf{U}}(t_k - t_{\text{ref}}) \quad (10)$$

A motion-compensated frame, or Image of Warped Events (IWE) I_{warp} , is generated by accumulating the counts of warped events into a 2D histogram (ignoring the polarities of each event):

$$I_{\text{warp}} = \sum_k^{N_e} \delta(\mathbf{x} - \mathbf{x}'_k) \quad (11)$$

where $\delta(\cdot)$ is the Dirac delta function and \mathbf{x} represents a pixel in the IWE. This process effectively integrates information over the batch into an image frame at any speed, creating a sharper representation of the Braille dots.

From one such generated frame I_{warp} , we select a Region of Interest (ROI) corresponding to a single Braille cell location. This ROI, illustrated in Figure 6b, then undergoes an image processing pipeline to enhance dot visibility and reduce noise. The steps include: applying a bilateral filter for edge-preserving smoothing, using Contrast Limited Adaptive Histogram Equalization (CLAHE) to increase local contrast, performing binary thresholding to segment potential dots,

and applying morphological opening and closing operations to eliminate salt-and-pepper noise.

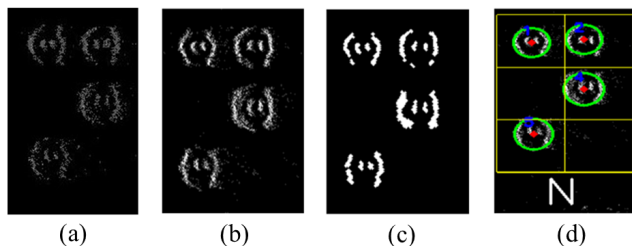


Fig. 6. Braille feature recognition pipeline applied on single letter ROI. (a) Direct accumulation of events (b) Motion compensated image of letter. (c) Denoised and processed letter image. (d) Hough transform applied and corresponding letter identified.

Following pre-processing, the cleaned ROI (cf. Figure 6c) is divided into the standard 2-column, 3-row Braille grid (6 squares). The Hough Circle Transform is then applied independently to each of the six squares to detect the presence or absence of a raised Braille dot. The detection results are encoded into a 6-bit binary vector, reading the grid from left-to-right, top-to-bottom, with '1' indicating a detected circle (dot) and '0' indicating its absence. This binary pattern is then compared against a Braille lookup table to identify the corresponding character (cf. Figure 6d). This pipeline, illustrated in Figure 6, enables the recognition of sequences of Braille characters directly from the high-speed tactile event data.

IV. EXPERIMENTAL SETUP

To evaluate the performance of the proposed neuromorphic roller tactile sensor, a series of experiments were conducted focusing on its capabilities in 3D surface reconstruction and tactile feature recognition under controlled conditions. The roller sensor was mounted as an end-effector onto a Universal Robots UR10 robotic arm, as depicted in Figure 7. This setup provided precise control over the linear rolling trajectory and speed of the sensor across various target surfaces, which is crucial for systematic evaluation and understanding the effect of operational parameters. The end effector velocity was recorded directly from the UR10 robot's real-time data interface and logged during the experiments. Experiments were conducted at various controlled speeds, ranging from 0.05 m/s to 0.5 m/s, allowing for analysis of the sensor's performance under different dynamic conditions.

A variety of objects and surfaces were utilized for testing:

- A calibrated metal sphere (4 mm radius) was used for parameter calibration and quantitative accuracy assessment of single-object reconstruction.
- Several 3D printed PLA objects with diverse geometries (e.g., stairs with fine gradations, sparse sphere (concentric circles) - see Fig. 8a.) were used to test the reconstruction capabilities on varied shapes.
- A larger 3D printed line array with varying heights (Fig. 8b) was employed to evaluate the sensor's performance in large surface reconstruction tasks involving stitching multiple frames.

- Standard Braille plates (Fig. 11) were used to assess the sensor's ability for high-speed fine feature detection and recognition.

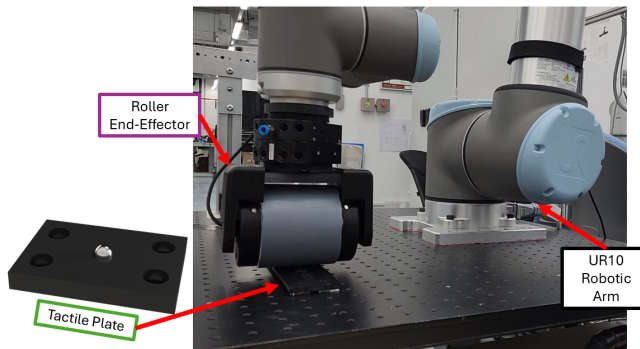


Fig. 7. Experimental setup showing the neuromorphic roller sensor mounted as an end-effector on a UR10 robotic arm. The robot controls the rolling motion over the mounted tactile plates.

The subsequent Results section (Sec. V) details the outcomes of these experiments. The evaluations focus on: (1) 3D reconstruction accuracy, primarily quantified using Mean Absolute Error (MAE) against ground truth geometries, including an analysis of the proposed BMA fusion strategy; (2) the relationship between rolling speed and reconstruction accuracy; (3) the effectiveness of large surface reconstruction through measurement stitching; and (4) the speed and accuracy achieved during high-speed Braille character recognition.

V. RESULTS

A. Single Object Reconstruction

As seen in Table III, the BMA fusion framework outperforms EMVS with an average percentage decrease in MAE of **25.2%** across all objects tested. Additionally, the fusion strategy of only fusing the left and right images that performed the best in reconstruction variability with Li et al. [53] was tested. While their method performs better than using the depth map generated using baseline EMVS, the proposed BMA fusion framework still outperforms the other methods. The depth maps generated for the single object reconstruction experiments in this comparison are shown in Figure 8a. Also, a qualitative analysis of the fusion strategy was conducted. A line array (3 identical rectangles with height 0.6 mm) was reconstructed using EMVS and BMA fusion framework. The pointclouds, depicted side-by-side in Figure 9, showcase a greater depth consistency and lower curvature warping when BMA is utilized. This visual improvement in consistency is confirmed quantitatively; the standard deviation of the reconstructed depth across the line array decreased significantly from 0.067 mm for the baseline EMVS reconstruction to 0.028 mm when using the BMA fusion approach, indicating a much more uniform depth estimation.

An analysis of the reconstruction accuracy across different object geometries (Table III) reveals a consistent performance trend: the sparse sphere yielded the lowest MAE,

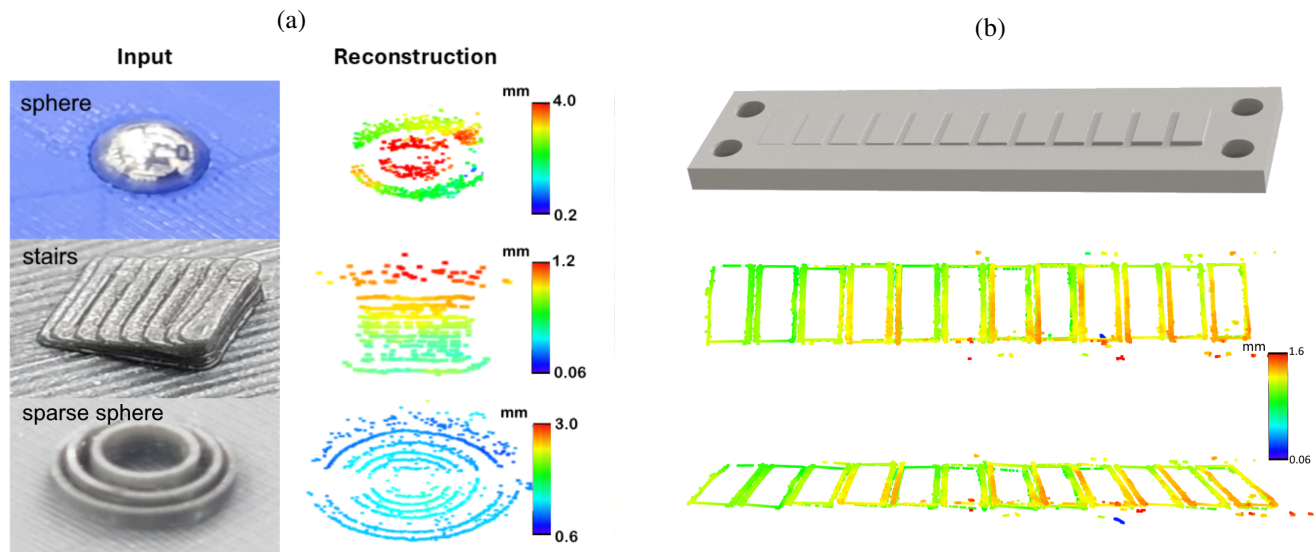


Fig. 8. Examples of 3D surface reconstruction results using the neuromorphic roller sensor. (a) Single object reconstruction (top view): 4mm sphere, 0.1mm stairs, sparse sphere. (b) Large surface reconstruction: 3D printed varying-height line array (top and isometric views).

TABLE III

EVALUATION OF THE TACTILE 3D RECONSTRUCTION AVERAGE MAE IN MM USING DIFFERENT DEPTH MAP FUSION WEIGHTS AT 0.3 M/S

Reconstruction Method	Stairs	Sphere	Sparse Sphere	Average
EMVS	0.0672	0.1256	0.0274	0.0734
Left & Right Fusion	0.0613	0.1085	0.0144	0.0614
BMA Fusion	0.0581	0.0946	0.0120	0.0549

followed by the stairs, with the solid sphere exhibiting the highest MAE. This trend correlates strongly with the operating principle of event cameras, which primarily generate signals at intensity edges during relative motion under consistent illumination. The sparse sphere presents distinct, well-separated edges with significant depth variance, facilitating robust event generation and accurate reconstruction. The stairs object, conversely, features numerous edges with smaller depth variations (0.1–0.2 mm) in close proximity, potentially leading to denser but possibly less distinct event clusters and increased reconstruction error. Finally, the solid sphere, possessing a smooth, continuous geometry without sharp edges (aside from the contact boundary), generates fewer internal feature-related events compared to the other objects (as suggested by the sparse sphere reconstruction in Fig. 8a), resulting in a sparser representation and consequently the highest reconstruction MAE among the tested shapes.

BMA also generated depth maps with lower MAE across varying speeds as illustrated in Figure 10 in comparison to EMVS and Left & Right Fusion. However, the reduction in the MAE of the sphere is more significant at higher speeds, with a 5.27% reduction at 0.05 m/s, a 25.2% reduction at 0.3 m/s and starts to plateau with a 26.4% reduction

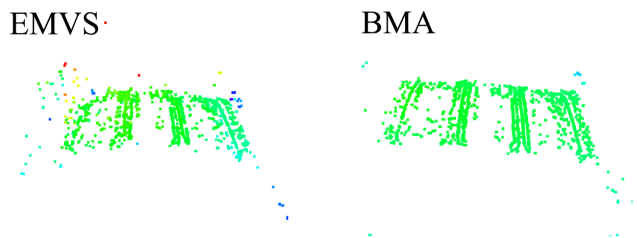


Fig. 9. Comparison of line array point cloud reconstruction for EMVS and BMA respectively. BMA pointcloud exhibits less noisy events and less curvature produced from cylindrical roller. Moreover, the MAE is lower by 25.2% when BMA fusion is used, highlighting decrease in depth inconsistency and curvature errors. Color represents change in depth using JET colormap.

at 0.5 m/s in comparison to EMVS. Interestingly, Figure 10 also shows that at lower speeds (e.g., 0.05 m/s), the performance difference between the BMA fusion (using all three reference views) and the Left & Right fusion (using only start and end views) becomes negligible. This suggests that while BMA fusion provides substantial benefits at higher speeds by effectively combining information from more distinct viewpoints to mitigate motion artifacts and improve consistency, at lower speeds the depth maps generated at the start, middle, and end times are likely very similar due to the minimal camera displacement within the time window. Consequently, fusing only the start and end views captures most of the available information, and adding the highly correlated midpoint view offers little additional advantage. These findings are in line with Bhattacharya et al. [58] as their event-based depth estimation model exhibits greater depth prediction quality at higher speeds. This effect could be explained by the fact that more events are generated within the same time window at higher speeds allowing for more accurate depth estimation through EMVS.

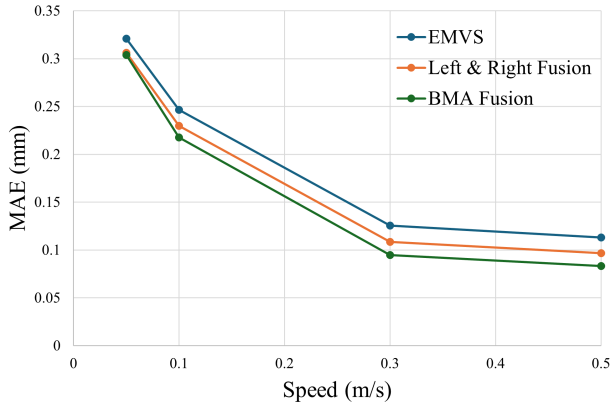


Fig. 10. Speed (m/s) against MAE (mm) for calibrated sphere comparing EMVS and BMA. MAE reduces as speed increases at exponentially decreasing rate.

B. Large Surface Reconstruction

The large surface reconstruction capabilities of our roller were tested with a 3D printed line array with varying heights (0.1-1.2 mm at intervals of 0.1 mm). The final point cloud is generated by aligning results from multiple depth maps as done by Zhang et al. [49]. The multiple depth maps are aligned using ICP; since the speed and hence the translation of the roller are known from the robotic controller, the translation along the rolling direction is used as the initial pose for ICP. The reconstruction results can be seen in Figure 8b with a resulting MAE of **0.0638 mm** across the whole surface. As aforementioned, speed is critical for large surface reconstruction using tactile sensing. Our roller exhibits, to the best of our knowledge, the highest measured speed at **0.5 m/s** or **500 mm/s** for tactile scanning with an MAE below **100 microns**. This is **11 times faster** than the maximum reported speed for rolling belt tactile sensors (45 mm/s) [26] and **45 times faster** than the highest speed for roller tactile sensors (11 mm/s) [24].

Table IV summarizes the performance trade-offs for different continuous tactile sensing approaches based on the provided documents. Our roller significantly advances the state-of-the-art in terms of speed, achieving 500 mm/s while maintaining a competitive 3D reconstruction accuracy (54.9 μm MAE). GelBelt demonstrates the potential for very high accuracy ($\sim 13.5 \mu\text{m}$ average MAE, measured against a high-resolution GelSight Max scan as ground truth for specific defects) but operates at a considerably lower maximum speed of 45 mm/s [26]. The GelRoller paper focused on a novel self-supervised reconstruction method, achieving 175 μm MAE in single-frame tests, but did not report a maximum scanning speed [49]. TouchRoller operated at the slowest speed (11 mm/s) and was designed for 2D texture mapping, not 3D reconstruction [24].

C. High-Speed Tactile Braille Reading

The large surface tactile scanning of the roller was also tested with regards to feature detection and recognition. Two

TABLE IV
COMPARISON BETWEEN TACTILE BELT/ROLLER SENSOR PERFORMANCE

Sensor	Max Reported Speed (mm/s)	MAE (μm)
GelBelt	45	~ 13.5
GelRoller	—	175
TouchRoller	11	—
Ours	500	<u>54.9</u>

braille plates were scanned with standard braille sizing: semi sphere of radius of 0.635 mm and spacing of 2.54 mm. The processing pipeline in Section III-F was utilized to process the events into a frame and subsequently detect the letter in the frame. Each frame is then stitched to the next frame to form the complete words (as seen in Figure 11 and Figure 1). Due to the high temporal resolution (microsecond resolution) of the event camera, the recognition algorithm performs well at low and high speeds (0.05 to 0.5 m/s). Utilizing the formula presented by Potdar et al. [23] for converting from m/s to wpm, our roller performs braille reading at **831 wpm** without loss in accuracy, which is **2.6 times faster** than the speed they demonstrate at 87.5% accuracy. Furthermore, as Potdar et al. highlight, this tactile feature recognition pipeline can be extended for dynamic detection of surface textures [23].

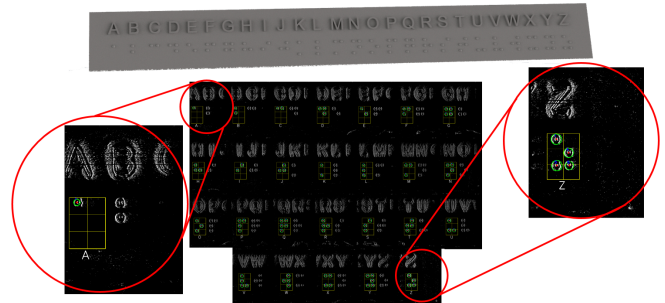


Fig. 11. High-speed braille reading. Tactile braille plate (top) and detected letters grid (bottom).

VI. CONCLUSION

In this work, we introduced a novel high-speed neuromorphic vision-based roller tactile sensor designed for continuous large surface inspection, addressing the speed limitations inherent in conventional VBTS technologies. We presented the sensor's mechanical design, integrating an event camera within a rolling elastomer mechanism, and developed a 3D reconstruction pipeline. This pipeline adapts the event-based multi-view stereo (EMVS) method and incorporates a Bayesian Model Averaging (BMA) fusion strategy, combining depth information from multiple reference viewpoints within a temporal window to enhance accuracy and robustness.

Our experimental results demonstrate the significant capabilities of the proposed system. We achieved state-of-the-art continuous tactile scanning speeds of up to 0.5 m/s for 3D surface reconstruction, yielding Mean Absolute Errors (MAE) below 100 microns on large surface tasks. This speed represents a substantial leap, being approximately 11 times faster than reported belt-based sensors and 45 times faster than previous roller-based VBTSSs. The BMA fusion technique proved crucial, reducing reconstruction MAE by an average of 25.2% compared to standard EMVS. Furthermore, leveraging the sensor's high temporal resolution, we demonstrated Braille character recognition at 831 words per minute, 2.6 times faster than the current benchmark for tactile Braille reading. These findings underscore the potential of neuromorphic vision to revolutionize high-speed tactile inspection, enabling applications previously infeasible due to the speed constraints of traditional methods, particularly in large-scale industrial quality control for aerospace or automotive components.

Despite the promising performance, the current approach exhibits limitations. The depth maps generated by the EMVS algorithm, relying on ray-counting from asynchronous and sparse event streams, are inherently semi-dense. While this works well for reconstructing objects with distinct edges or sufficient texture to generate events, it can struggle with accurately capturing smooth, continuous surface geometries where event generation might be sparse, potentially leading to incomplete or interpolated reconstructions. Moreover, the event camera used, the DVXplorer mini, has a resolution of 640x480 pixels (VGA). This inherently limits the spatial resolution achievable by the roller tactile sensor. Currently, event camera technology is less mature than conventional camera technology. As the field advances, future event cameras with higher resolutions are expected. Integrating these improved cameras would significantly enhance the spatial resolution of our sensor design.

Future research will focus on addressing these limitations and expanding the sensor's capabilities. Firstly, we plan to investigate the integration of force and contact angle sensing and control. This could involve adding markers to the non-sensing sides of the roller, using their displacement within a learning-based framework to estimate applied force and roller orientation relative to the surface. Implementing closed-loop control based on this feedback would ensure consistent contact, which is crucial for maintaining high-quality tactile data acquisition, especially on non-planar surfaces. Secondly, to overcome the challenges associated with sparse depth maps from EMVS, we aim to explore alternative event-based reconstruction methods capable of generating denser surface information. Techniques such as event-based structured light measurement or event-based photometric stereo could potentially be adapted to the tactile roller geometry to directly estimate dense surface normals or depth maps from the event data. Achieving denser reconstructions would significantly enhance the sensor's ability to accurately measure complex, continuously varying surface geometries, broadening its applicability.

REFERENCES

- [1] M. Futterlieb, J. Frejaville, F. Donadio, M. Devy, and S. Larnier, "Aircobot: Aircraft enhanced inspection by smart and collaborative robot," 2017.
- [2] Y. Abdulrahman, M. A. M. Eltoum, A. Ayyad, B. Moyo, and Y. Zweiri, "Aero-engine blade defect detection: A systematic review of deep learning models," *IEEE Access*, vol. 11, pp. 53 048–53 061, 2023.
- [3] W. Yuan, S. Dong, and E. H. Adelson, "Gelsight: High-resolution robot tactile sensors for estimating geometry and force," *Sensors*, vol. 17, no. 12, p. 2762, 2017.
- [4] A. Agarwal, A. Ajith, C. Wen, V. Stryzheus, B. Miller, M. Chen, M. K. Johnson, J. L. S. Rincon, J. Rosca, and W. Yuan, "Robotic defect inspection with visual and tactile perception for large-scale components," in *2023 IEEE/RSJ International Conference on Intelligent Robots and Systems (IROS)*. IEEE, 2023, pp. 10 110–10 116.
- [5] V. Sekatskii, O. Gavrilova, N. Merzlikina, and V. Morgun, "Analysis of techniques for verification of coating thickness gauges," *Measurement Techniques*, vol. 62, no. 9, pp. 762–768, 2019.
- [6] J. S. Villarrubia, "Algorithms for scanned probe microscope image simulation, surface reconstruction, and tip estimation," *Journal of research of the National Institute of Standards and Technology*, vol. 102, no. 4, p. 425, 1997.
- [7] P. Russell, D. Batchelor, and J. Thornton, "Sem and afm: complementary techniques for high resolution surface investigations," *AN46, Rev A*, vol. 1, 2001.
- [8] S. Yang and G. Zhang, "A review of interferometry for geometric measurement," *Measurement Science and Technology*, vol. 29, no. 10, p. 102001, 2018.
- [9] J. Jonkman, C. M. Brown, G. D. Wright, K. I. Anderson, and A. S. North, "Tutorial: guidance for quantitative confocal microscopy," *Nature protocols*, vol. 15, no. 5, pp. 1585–1611, 2020.
- [10] M. Salah, A. Ayyad, M. Ramadan, Y. Abdulrahman, D. Swart, A. Abusafieh, L. Seneviratne, and Y. Zweiri, "High speed neuromorphic vision-based inspection of countersinks in automated manufacturing processes," *Journal of Intelligent Manufacturing*, vol. 35, no. 7, pp. 3067–3081, 2024.
- [11] L. Deng, G. Liu, and Y. Zhang, "A review of machine vision applications in aerospace manufacturing quality inspection," in *2024 4th International Conference on Computer, Control and Robotics (ICCCR)*. IEEE, 2024, pp. 31–39.
- [12] R. Gregory, "Production inspection of aerospace composites using laser shearography," *Insight - Non-Destructive Testing and Condition Monitoring*, vol. 44, pp. 220–223, 2002.
- [13] S. Zhang, "High-speed 3d shape measurement with structured light methods: A review," *Optics and lasers in engineering*, vol. 106, pp. 119–131, 2018.
- [14] M. Ramadan, A. Youssef, A. Ayyad, L. AbuAssi, O. A. Hay, M. Salah, B. Moyo, Y. Zweiri, and Y. Abdulrahman, "Vision-guided robotic system for aero-engine inspection and dynamic balancing," *Scientific Reports*, vol. 14, no. 1, p. 30742, Dec. 2024.
- [15] G. Häusler and S. Ettl, *Limitations of Optical 3D Sensors*. Berlin, Heidelberg: Springer Berlin Heidelberg, 2011, pp. 23–48.
- [16] M. K. Johnson and E. H. Adelson, "Surface metrology using an elastomeric sensor," in *Imaging and Applied Optics*. Optica Publishing Group, 2011, p. AITuB4.
- [17] Q. Li, O. Kroemer, Z. Su, F. F. Veiga, M. Kaboli, and H. J. Ritter, "A review of tactile information: Perception and action through touch," *IEEE Transactions on Robotics*, vol. 36, no. 6, pp. 1619–1634, 2020.
- [18] S. Dong, W. Yuan, and E. H. Adelson, "Improved gelsight tactile sensor for measuring geometry and slip," in *2017 IEEE/RSJ International Conference on Intelligent Robots and Systems (IROS)*, 2017, pp. 137–144.
- [19] E. Donlon, S. Dong, M. Liu, J. Li, E. Adelson, and A. Rodriguez, "Gelslim: A high-resolution, compact, robust, and calibrated tactile-sensing finger," in *2018 IEEE/RSJ International Conference on Intelligent Robots and Systems (IROS)*. IEEE, 2018, pp. 1927–1934.
- [20] S. Q. Liu and E. H. Adelson, "Gelsight fin ray: Incorporating tactile sensing into a soft compliant robotic gripper," in *2022 IEEE 5th International Conference on Soft Robotics (RoboSoft)*. IEEE, 2022, pp. 925–931.
- [21] J. Zhao and E. H. Adelson, "Gelsight svelte: A human finger-shaped single-camera tactile robot finger with large sensing coverage and proprioceptive sensing," in *2023 IEEE/RSJ International Conference on Intelligent Robots and Systems (IROS)*. IEEE, 2023, pp. 8979–8984.

- [22] J. Xu, W. Chen, H. Qian, D. Wu, and R. Chen, "Thintact: Thin vision-based tactile sensor by lensless imaging," *IEEE Transactions on Robotics*, vol. 41, pp. 1139–1154, 2025.
- [23] P. Potdar, D. Hardman, E. Almanzor, and F. Iida, "High-Speed Tactile Braille Reading via Biomimetic Sliding Interactions," *IEEE Robotics and Automation Letters*, vol. 9, no. 3, pp. 2614–2621, Mar. 2024.
- [24] G. Cao, J. Jiang, C. Lu, D. F. Gomes, and S. Luo, "Touchroller: A rolling optical tactile sensor for rapid assessment of textures for large surface areas," *Sensors*, vol. 23, no. 5, p. 2661, 2023.
- [25] K. Shimonomura, T. Chang, and T. Murata, "Detection of foreign bodies in soft foods employing tactile image sensor," *Frontiers in Robotics and AI*, vol. 8, p. 774080, 2021.
- [26] M. A. Mirzaee, H.-J. Huang, and W. Yuan, "GelBelt: A Vision-Based Tactile Sensor for Continuous Sensing of Large Surfaces," *IEEE Robotics and Automation Letters*, vol. 10, no. 2, pp. 2016–2023, 2025.
- [27] Z. Li, Z. Zou, W. Xu, Y. Zhou, G. Zhou, M. Huang, X. Huang, and X. Li, "Cyclic fusion of measuring information in curved elastomer contact via vision-based tactile sensing," *IEEE Transactions on Instrumentation and Measurement*, vol. 74, pp. 1–11, 2025.
- [28] G. Gallego, T. Delbrück, G. Orchard, C. Bartolozzi, B. Taba, A. Censi, S. Leutenegger, A. J. Davison, J. Conradt, K. Daniilidis, and D. Scaramuzza, "Event-based vision: A survey," *IEEE Transactions on Pattern Analysis and Machine Intelligence*, vol. 44, no. 1, pp. 154–180, 2022.
- [29] X. Huang, Y. Zweiri, L. Seneviratne, and D. Gan, "Real-time grasping strategies using event camera," *Journal of Intelligent Manufacturing*, vol. 33, no. 2, pp. 593–615, 2022.
- [30] C. Brandli, R. Berner, M. Yang, S.-C. Liu, and T. Delbruck, "A 240 × 180 130 db 3 μs latency global shutter spatiotemporal vision sensor," *IEEE Journal of Solid-State Circuits*, vol. 49, no. 10, pp. 2333–2341, 2014.
- [31] C. Posch, D. Matolin, and R. Wohlgenannt, "A qvga 143 db dynamic range frame-free pwm image sensor with lossless pixel-level video compression and time-domain cds," *IEEE Journal of Solid-State Circuits*, vol. 46, no. 1, pp. 259–275, 2011.
- [32] P. Lichtsteiner, C. Posch, and T. Delbruck, "A 128 × 128 120 db 15 μs latency asynchronous temporal contrast vision sensor," *IEEE Journal of Solid-State Circuits*, vol. 43, no. 2, pp. 566–576, 2008.
- [33] N. Funk, E. Helmut, G. Chalvatzaki, R. Calandra, and J. Peters, "Eventac: An event-based optical tactile sensor for robotic manipulation," *IEEE Transactions on Robotics*, vol. 40, pp. 3812–3832, 2024.
- [34] B. Ward-Cherrier, N. Pestell, and N. F. Lepora, "Neurotac: A neuro-morphic optical tactile sensor applied to texture recognition," in *2020 IEEE International Conference on Robotics and Automation (ICRA)*. IEEE, 2020, pp. 2654–2660.
- [35] H. Sajwani, A. Ayyad, Y. Alkendi, M. Halwani, Y. Abdulrahman, A. Abusafieh, and Y. Zweiri, "Tactigraph: An asynchronous graph neural network for contact angle prediction using neuromorphic vision-based tactile sensing," *Sensors*, vol. 23, no. 14, 2023.
- [36] O. Faris, R. Muthusamy, F. Renda, I. Hussain, D. Gan, L. Seneviratne, and Y. Zweiri, "Proprioception and exteroception of a soft robotic finger using neuromorphic vision-based sensing," *Soft Robotics*, vol. 10, no. 3, pp. 467–481, 2023.
- [37] M. Salah, I. Mohamed Zaid, M. Halwani, H. Sajwani, A. Solayman, A. Ayyad, R. Azzam, A. Abusafieh, and Y. Zweiri, "Neutac: Zero-shot sim2real measurement for neuromorphic vision-based tactile sensors," *IEEE Transactions on Instrumentation and Measurement*, vol. 73, pp. 1–15, 2024.
- [38] J. Salvi, J. Pagès, and J. Batlle, "Pattern codification strategies in structured light systems," *Pattern recognition*, vol. 37, no. 4, pp. 827–849, 2004.
- [39] G. Sansoni, M. Trebeschi, and F. Docchio, "State-of-the-art and applications of 3d imaging sensors in industry, cultural heritage, medicine, and criminal investigation," *Sensors*, vol. 9, no. 1, pp. 568–601, 2009.
- [40] L. Laser, "The new edition of the international laser product safety standard iec 60825-1," *laser*, vol. 43, no. 50550, p. 2882, 2017.
- [41] A. Agarwal, T. Man, and W. Yuan, "Simulation of vision-based tactile sensors using physics based rendering," in *2021 IEEE International Conference on Robotics and Automation (ICRA)*. IEEE, 2021, pp. 1–7.
- [42] S. Wang, M. Lambeta, P.-W. Chou, and R. Calandra, "Tacto: A fast, flexible, and open-source simulator for high-resolution vision-based tactile sensors," *IEEE Robotics and Automation Letters*, vol. 7, no. 2, pp. 3930–3937, 2022.
- [43] I. Akinola, J. Xu, J. Carius, D. Fox, and Y. Narang, "Tactsl: A library for visuotactile sensor simulation and learning," *IEEE Transactions on Robotics*, vol. 41, pp. 2645–2661, 2025.

- [44] S. Zhong, A. Albin, P. Maiolino, and I. Posner, "Tactgen: Tactile sensory data generation via zero-shot sim-to-real transfer," *IEEE Transactions on Robotics*, vol. 41, pp. 1316–1328, 2025.
- [45] GelSight Inc., "GelSight Mobile™ Series 2 Product Sheet," Online, October 2024.
- [46] F. Baghaei Naeini, E. A. Asl, A. Heydari, S. E. Khadem, S. Aghaeifar, and N. Navab, "A novel dynamic-vision-based approach for tactile sensing applications," *IEEE Transactions on Instrumentation and Measurement*, vol. 69, no. 5, pp. 1881–1893, 2020.
- [47] M. Lepert, C. Pan, S. Yuan, R. Antonova, and J. Bohg, "In-hand manipulation of unknown objects with tactile sensing for insertion," in *Embracing Contacts-Workshop at ICRA 2023*, 2023.
- [48] S. Yuan, S. Wang, R. Patel, M. Tippur, C. L. Yako, M. R. Cutkosky, E. Adelson, and J. K. Salisbury, "Tactile-reactive roller grasper," *IEEE Transactions on Robotics*, vol. 41, pp. 1938–1955, 2025.
- [49] Z. Zhang, H. Ma, Y. Zhou, J. Ji, and H. Yang, "GelRoller: A Rolling Vision-based Tactile Sensor for Large Surface Reconstruction Using Self-Supervised Photometric Stereo Method," in *2024 IEEE International Conference on Robotics and Automation (ICRA)*, May 2024, pp. 7961–7967.
- [50] R. T. Collins, "A space-sweep approach to true multi-image matching," *Proceedings CVPR IEEE Computer Society Conference on Computer Vision and Pattern Recognition*, pp. 358–363, 1996.
- [51] H. Rebecq, G. Gallego, E. Mueggler, and D. Scaramuzza, "Emvs: Event-based multi-view stereo—3d reconstruction with an event camera in real-time," *International Journal of Computer Vision*, vol. 126, pp. 1394–1414, 2017.
- [52] A. Ayyad, M. Halwani, D. Swart, R. Muthusamy, F. Almaskari, and Y. Zweiri, "Neuromorphic vision based control for the precise positioning of robotic drilling systems," *Robotics and Computer-Integrated Manufacturing*, vol. 79, p. 102419, 02 2023.
- [53] Z. Li, Z. Zou, W. Xu, Y. Zhou, G. Zhou, M. Huang, X. Huang, and X. Li, "Cyclic fusion of measuring information in curved elastomer contact via vision-based tactile sensing," *IEEE Transactions on Instrumentation and Measurement*, pp. 1–1, 01 2025.
- [54] S. Shiba, Y. Klose, Y. Aoki, and G. Gallego, "Secrets of event-based optical flow, depth and ego-motion estimation by contrast maximization," *IEEE Transactions on Pattern Analysis and Machine Intelligence*, vol. 46, pp. 7742–7759, 05 2024.
- [55] J. Sun, F. J. Quevedo, and E. Bollt, "Bayesian optical flow with uncertainty quantification," *Inverse Problems*, vol. 34, p. 105008, 2018.
- [56] M. Salah, A. Ayyad, M. Humais, D. Gehrig, A. Abusafieh, L. Seneviratne, D. Scaramuzza, and Y. Zweiri, "E-calib: A fast, robust, and accurate calibration toolbox for event cameras," *IEEE Transactions on Image Processing*, vol. 33, pp. 3977–3990, 2024.
- [57] G. Gallego, H. Rebecq, and D. Scaramuzza, "A unifying contrast maximization framework for event cameras, with applications to motion, depth, and optical flow estimation," in *2018 IEEE/CVF Conference on Computer Vision and Pattern Recognition*, 2018, pp. 3867–3876.
- [58] A. Bhattacharya, M. Cannici, N. Rao, Y. Tao, V. Kumar, N. Matni, and D. Scaramuzza, "Monocular event-based vision for obstacle avoidance with a quadrotor," in *8th Annual Conference on Robot Learning*, 2024.